ACTA METALLURGICA SLOVACA
2024, VOL. 30, NO. 3, 127-132

RESEARCH PAPER

SYNTHESIS OF ORTHORHOMBIC $LiMnO_2$ BY HYDROTHERMAL PROCESS

Binh Ngoc Duong[1,], Thang Van Pham[1], Hung Tuan Hoang[1], Thang Hong Le[1], Huy Duc Tran[1]*

[1] School of Materials Science and Engineering, Hanoi University of Science and Technology, No. 1, Dai Co Viet, Hai Ba Trung, Hanoi, Vietnam

*Corresponding author: binh.duongngoc@hust.edu.vn, tel.: +84 973002988, School of Materials Science and Engineering/Hanoi University of Science and Technology, Hanoi, Vietnam

Received: 23.07.2024
Accepted: 03.09.2024

ABSTRACT

This work synthesised layered structural orthorhombic $LiMnO_2$ powder via a hydrothermal process. The influences of hydrothermal temperature ($t_r°$), reaction time (t_{ht}), molar concentration of $LiOH.H_2O$ in aqueous solutions (C_{LH}), and the ratio of Mn_2O_3 powder ($x_{r/t}$) were investigated. A high-purity $LiMnO_2$ powder was successfully synthesised using hydrothermal synthesis at C_{LH} = 4M, t_{ht} = 8 h, $t_r°$ = 180 °C, and $x_{r/t}$ = 0.9. The synthesis $LiMnO_2$ powders have layer structure, and the planar density calculations indicated that the (021) planes had a lower average planar density than those of (100) and (010) planes, which led to a faster crystal growth on (021) planes. Moreover, single crystals of $LiMnO_2$ were pseudo-hexagonal also due to the lower average planar density of (221) planes compared to that of (021) planes, which made the crystal grow faster on (221) planes.

Keywords: $LiMnO_2$; cathode material; hydrothermal synthesis

INTRODUCTION

With the global shortage of energy, the pollution of fossil-fuel manufacture, and the high cost, as well as the instability of green energy sources such as solar, wind, and ocean power, lithium-ion batteries (LIBs) have emerged and been still applied widely as a sustainable power source for most of portable electronic devices such as smartphones, laptops, digital cameras, tablets, wearable devices, and even for transportation nowadays. Among cathode materials in commercial batteries, $LiCoO_2$ is considered the most successful positive electrode material with ease of synthesis, high theoretical capacity, excellent capacity retention and reliability [1, 2]. Nevertheless, low energy density is one of the biggest hindering factors that makes $LiCoO_2$ less satisfied with the new electronic devices due to their ever-development [3]. Furthermore, because of the relatively high price, pollution, and human cost of cobalt mining and manufacture, the price of batteries using $LiCoO_2$ as their cathode material is elevated [4, 5]. These disadvantages have accelerated research community to find alternative positive electrode materials.

One of the practical candidates for LIBs is lithium manganese oxides, which have been researched and commercialized parallelly because of the abundance of manganese resources. Spinel lithium manganese dioxide ($LiMn_2O_4$) possesses remarkable advantages such as nontoxicity, high safety performance, low cost, eco-friendliness, structural stability, and relatively good capacity retention [6-11]. Unfortunately, $LiMn_2O_4$ indicates a low theoretically reversible capacity (148 $mAhg^{-1}$) that makes it mostly unable to satisfy the high-power applications, whereas this drawback has been solved with layered lithium manganese oxides ($LiMnO_2$). The theoretical capacity of layered lithium manganese oxides is up to 285 $mAhg^{-1}$ [12].

Because of the excellent electrochemical properties, there are many efforts to fabricate layered $LiMnO_2$ with the desire to approach its ideal performance. Armstrong et al. has successfully synthesized monoclinic $LiMnO_2$ (m-$LiMnO_2$) via ion exchange from refluxing $NaMnO_2$ with an excess of LiCl or LiBr in n-hexanol at 140-150 °C for 6-8 hours. The product exhibited 200 and 270 $mAhg^{-1}$ capacities at the current densities of 0.5 $mAcm^{-2}$ and 10 μAcm^{-2}, respectively [13]. Zhou et al. performed carbothermal reduction with LiOH and MnO_2 under Ar atmosphere at 450 °C or 600 °C for 15 h for the synthesis of m-$LiMnO_2$ [14]. Their products exhibited a high averaged coulombic efficiency of around 99% and good cycle stability with the B-doping effect. The non-doped sample showed a low coulombic efficiency of about 70% and failed after 20-30 cycles due to the poor cycling stability of m-$LiMnO_2$ [14, 15]. Orthorhombic $LiMnO_2$ (o-$LiMnO_2$) was fabricated via the sol-gel process from $Mn(CH_3COO)_2.4H_2O$, $Li(CH_3COO).2H_2O$, and citric acid, which was showed a high initial capacity of above 190 $mAhg^{-1}$ at a current density of 0.4 $mAcm^{-2}$ at room temperature [16]. Quenching method has been used to synthesize successfully o-$LiMnO_2$ using LiOH and γ-MnOOH at 1000 - 1050 °C in an argon flow, and the fabricated product has an energy density of 201 $mAhg^{-1}$ in the first cycle and exhibited a great capacity retention after 12 h grinding [17]. Guo et al. using the solid-state method also successfully fabricated o-$LiMnO_2$ at 800 °C with a high initial capacity of 180 $mAhg^{-1}$ at 0.5 $mAcm^{-2}$ [18]. Mechanical alloying method has been also performed to fabricate o-$LiMnO_2$ using Mn_2O_3 and $LiOH.H_2O$ as precursors [19]. Their best as-prepared sample was 220.3 $mAhg^{-1}$ and 185.9 $mAhg^{-1}$ as the initial charge and corresponding discharge capacity, respectively; nevertheless, its capacity retention was remarkably low [19]. There were also attempts to fabricate o-$LiMnO_2$ via hydrothermal process at distinct temperature ranges, but detailed

investigations of material synthesis were absent with variation of properties [20-22].
In this work, the synthesis of o-$LiMnO_2$ via a hydrothermal process at low temperatures using lithium hydroxide monohydrate ($LiOH.H_2O$) and manganese (III) oxide (Mn_2O_3) as precursors was investigated. The effect of variations such as hydrothermal temperature, reaction time, molar concentration of $LiOH.H_2O$, and the amount of Mn_2O_3 available for reaction was studied in detail.

MATERIAL AND METHODS

Lithium hydroxide monohydrate ($LiOH.H_2O$) and manganese (III) oxide (Mn_2O_3) were used as the starting materials for the synthesis of o-$LiMnO_2$. Lithium hydroxide monohydrate, and manganese dioxide powder was obtained from Macklin, China, had a purity of 98%, and 99%, respectively. The starting Mn_2O_3 was fabricated by calcinating the commercial manganese dioxide (MnO_2). The calcination of MnO_2 was performed at 800 °C for 2, 5, and 8 h in air. The amount of MnO_2 was weighed according to the stoichiometric ratio of the reaction:

$$4MnO_2 = 2Mn_2O_3 + O_2 \quad (1.)$$

The Mn_2O_3 powder was added to a $LiOH.H_2O$ aqueous solution in a 25ml Teflon autoclave. To fabricate a desired amount of o-$LiMnO_2$, the amounts of $LiOH.H_2O$ and Mn_2O_3 were controlled by the reaction:

$$Mn_2O_3 + 2LiOH.H_2O = 2LiMnO_2 + 3H_2O \quad (2.)$$

The autoclave then heated at desired temperature for a specific duration to completing the reaction. The hydrothermal process was investigated via four variables including hydrothermal temperature (160, 180, 200, 220, and 240 °C), reaction time (2, 4, 6, 8, 10, and 12 h), molar concentration of $LiOH.H_2O$ in aqueous solutions (2M, 4M, and 6M), and the amount of Mn_2O_3 available for reaction (90, 95, and 100% according to reaction 2). After hydrothermal process, the products were filtered and dried at 80 °C for 7 h in air. A schematic diagram of the experimental process is shown in **Fig. 1**.

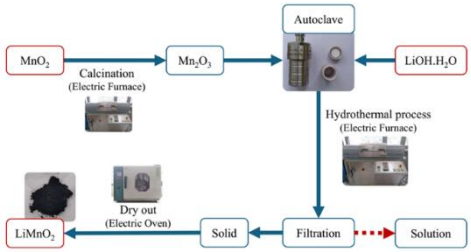

Fig. 1 Schematic diagram of the experimental process

The phase characterization of the powders was performed using X-ray diffraction analysis (XRD, PANalytical Aeris, Netherlands). The surface morphologies and microstructure were characterized by scanning electron microscopy (SEM, JEOL JSM-IT200, Japan).

RESULTS AND DISCUSSION

3.1. Calcination of MnO_2

The XRD patterns of the commercial precursor MnO_2 and the obtained sample after calcination at 800 °C for 2, 5 and 8 hours are shown in **Fig. 2**. The peaks in the MnO_2 pattern can be indexed to an orthorhombic phase (PDF No. 82-2169). Meanwhile, all peaks in the Mn_2O_3 patterns are indexed to cubic Mn_2O_3 (PDF No. 76-0150). As reported in previous works, MnO_2 can be converted into Mn_2O_3 at high temperature [23, 31]. The results indicated that after calcination at 800 °C, the MnO_2 has completely converted into Mn_2O_3. There was no MnO_2 detected in the calcinated powders.

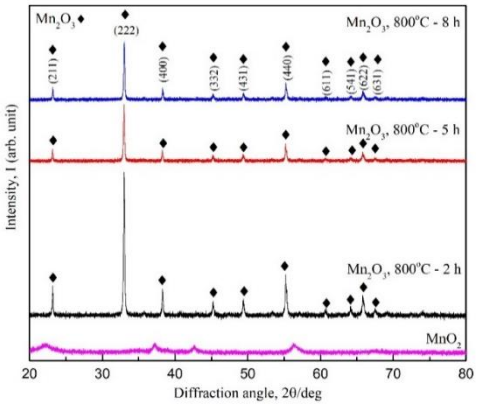

Fig. 2 XRD patterns of precursor MnO_2 and calcinated Mn_2O_3

3.2. Synthesis of $LiMnO_2$

In the first series of experiments, the amount of Mn_2O_3 used was 100% according to the stoichiometric amount required in reaction (2), the synthesis temperature was 200 °C and the time was 2 h. XRD patterns of the samples synthesized at different molar concentrations of $LiOH.H_2O$ (C_{LH}) from 2, 4 and 6 M are shown in **Fig. 3**.
The XRD patterns indicate that at C_{LH} = 2 M, the product was a mixture of o-$LiMnO_2$ (PDF No. 35-0749) and Mn_2O_3. There was some remaining Mn_2O_3 in the product as the main peaks of Mn_2O_3 appeared at 32.9° and 55.2°. Increasing the value of C_{LH} to 4 M leads to the intensity of Mn_2O_3 peaks being significantly reduced. It can be concluded that more Mn_2O_3 has been reacted to form o-$LiMnO_2$ when more $LiOH.H_2O$ was added. There was a remarkable increase in the intensities of o-$LiMnO_2$ peaks at 15.4°, 39.3°, 45.1°, and 61.3°, which could be caused by an increase in interaction between $LiOH.H_2O$ and Mn_2O_3 as more $LiOH.H_2O$ was available for reaction.
However, when C_{LH} was increased to 6 M, there was only a small difference between the intensity of Mn_2O_3 phase compared to those obtained at C_{LH} = 4 M. It was likely caused by the low solubility of Mn_2O_3 at the hydrothermal conditions (200 °C), only a certain amount of Mn_2O_3 was dissolved and reacted with $LiOH.H_2O$. The low solubility of Mn_2O_3 at relatively low temperature was also reported in previous research. In an attempt to synthesize o-$LiMnO_2$ at 170 °C for a relatively long time (4 days), Mn_2O_3 was found to have low solubility and also, $Mn(OH)_2$ was seen as a side product in the hydrothermal process [24, 25]. In all three cases, Mn_2O_3 remained the main impurity in the synthesized o-$LiMnO_2$.

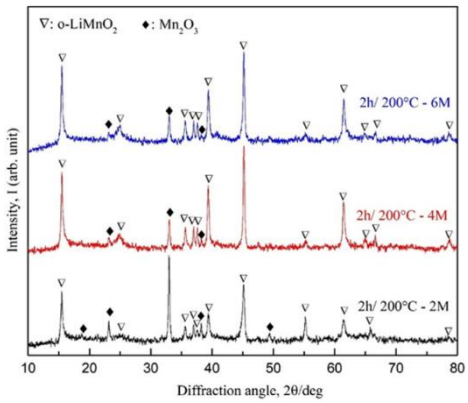

Fig. 3 XRD patterns of $LiMnO_2$ synthesized at different $LiOH.H_2O$ molar concentrations

In the next series of experiments, 100% Mn_2O_3 was used, the C_{LH} was fixed at 2 M, and the reaction duration was 2 h. The reaction temperature varied from 160 to 240 C, and the XRD patterns of the obtained sample are shown in **Fig. 4**.

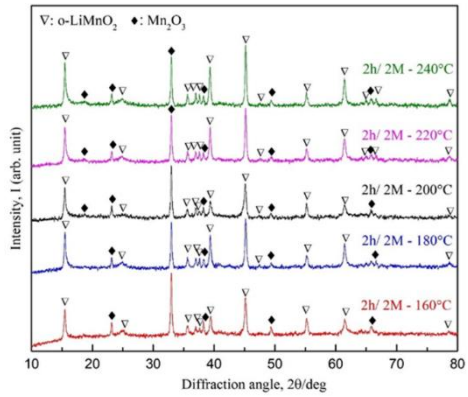

Fig. 4 XRD patterns of $LiMnO_2$ synthesized at different temperature

It can be seen that at 160 °C, although o-$LiMnO_2$ is formed but the intensity of the $LiMnO_2$ peaks were relatively low, which indicates low efficiency of the formation reaction. Temperature increases up to 240 °C do not significantly improve the situation as there was only a small difference between the XRD peaks. Therefore, it can be suggested that hydrothermal synthesis of o-$LiMnO_2$ is inefficient at low temperatures. To improve the reaction efficiency, different raw materials could be used for the synthesis of o-$LiMnO_2$ [15]. It is reported that o-$LiMnO_2$ could be synthesized efficiently at relatively low temperature using Mn_2O_3 and LiCl as precursors, and KOH as a solution. However, it might lead to the formation of monoclinic $LiMnO_2$ phase (m-$LiMnO_2$) in parallel with the formation of o-$LiMnO_2$ [15].

Fig. 5 shows the XRD patterns of the sample produced at different hydrothermal times from 2 to 12 h. The experiment conditions were prefixed at C_{LH} = 2 M, 200 °C and 100% of Mn_2O_3.

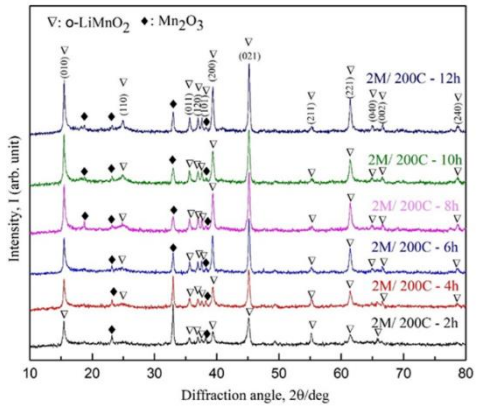

Fig. 5 XRD patterns of $LiMnO_2$ synthesized at different time

The result indicates a low reaction efficiency in the first sample with a reaction time of 2 h. The reaction efficiency improves remarkably as the reaction time increases up to 8 h and remain almost the same after that. The report of Su and Wang [15] also showed a similar behavior in which the reaction efficiency of $LiMnO_2$ formation was significantly improved when increasing reaction time from 2 to 4 h. The high pH value of hydrothermal solution were likely the reasons to achieve high reaction efficiency in a shorter reaction time [15].

Fig. 6 shows the Rietveld refinement patterns of obtained $LiMnO_2$ samples at 180 °C, C_{LH} = 4 M and the reaction time was 8 h, the amount of Mn_2O_3 used was 100%, 95% and 90%, respectively. Rietveld refinement was performed by the Fullprof Suite software (version 8.00), Crystallographic information files (CIFs) of $LiMnO_2$ and Mn_2O_3 were obtained from the Crystallography Open Database (COD). The corresponding values of the goodness of fit χ^2, the profile residual R_p, the weighted profile residual R_{wp}, and the expected R-factor R_{exp} are shown in Table 1. These factors are defined by the equations in which R_p and R_{wp} describe the difference between the experimental observations and the ideal calculated values, R_{exp} is the "best possible R_{wp}" quantity, and χ is the goodness of fit [32, 34].

Table 1. The goodness of fit χ^2, the profile residual R_p, and the weighted profile residual R_{wp} for Rietveld refinement of $LiMnO_2$ samples with $x_{r/t}$ = 1, 0.95, and 0.9.

$x_{r/t}$	χ^2	R_p	R_{wp}	R_{exp}
1	1.18	1.80	2.26	2.08
0.95	1.17	1.77	2.23	2.06
0.9	1.25	1.80	2.28	2.04

In this work, the least-squares minimization method used for Rietveld analysis, the weight w_i can be estimated to $w_i = 1/\sigma^2[y_{O,i}]$ where $\sigma[y_{O,i}]$ is the uncertainty of the observed intensity $y_{O,i}$ [32, 33]. When the minimized differences between the observed and computed intensity values $(y_{C,i} - y_{O,i})^2$ are high, it means the uncertainties are high, which in turn make the weight values small, and therefore, reduce the impact of those data points on the overall fit. Likewise, the weight values will promote the impact of the data points with lower uncertainties on the overall fit. Visually, in **Fig. 6a-6c**, the fitting quality between the observed and computed profiles was pretty good except the poor fit at about 15.5° and 45° due to the preferred orientation effect.

As shown in **Fig. 6** on the observed patterns (the red plots), the main peaks of Mn_2O_3 at 32.95° and 23.1° almost disappeared, which was shown the high purity of these samples. Fig. 6d shows

the variation of the residual Mn_2O_3 in three samples with different amount of Mn_2O_3 added ($x_{r/t}$). The results indicated that the reduction of the Mn_2O_3 amount used obviously increased quality of the $LiMnO_2$-product. The residual weight percentage of Mn_2O_3 reduced from 1.94% to 0.24% as $x_{r/t}$ reduced from 100% to 90%.

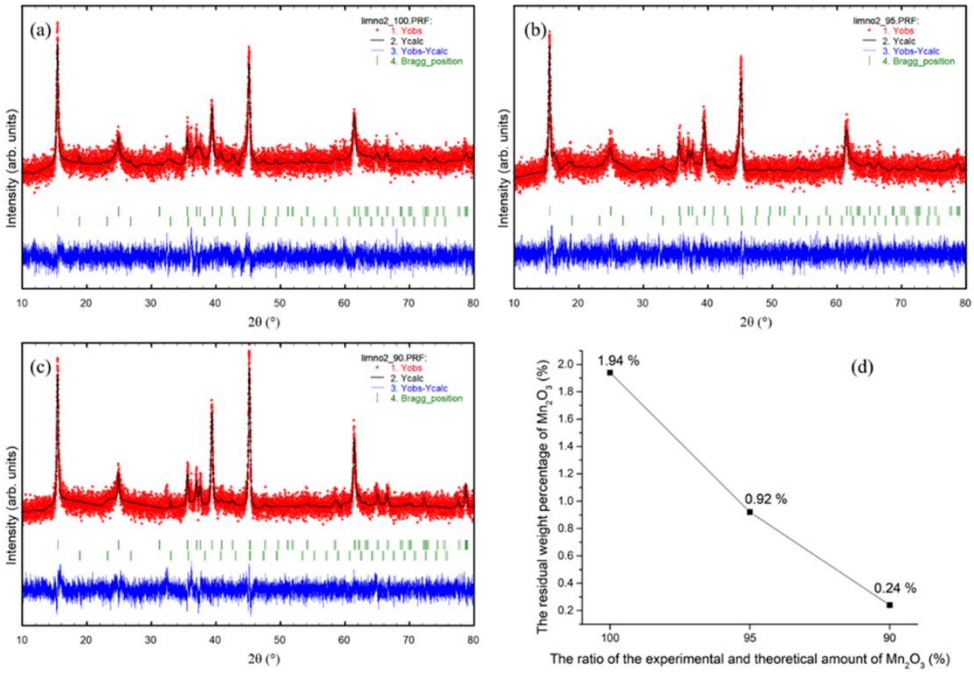

Fig. 6 Rietveld refinement patterns of $LiMnO_2$ samples with a) 100% Mn_2O_3, b) 95% Mn_2O_3, c) 90% Mn_2O_3; and (d) is the residual weight percentage of Mn_2O_3.

3.3 Crystal structure of synthesized o-$LiMnO_2$

Fig. 7 shows the SEM images of o-$LiMnO_2$ synthesized after 10 h of reaction time at 200 °C and C_{LH} = 2M. It can be suggested that the o-$LiMnO_2$ was formed in a pseudo-hexagonal shape.

Structural modelling of o-$LiMnO_2$ synthesized after 10 h was performed using the VESTA software (version 3.5.4). Crystallographic information files (CIFs) of $LiMnO_2$ were obtained from the Crystallography Open Database (COD). The lattice parameters of $LiMnO_2$ at 200°C, C_{LH} = 2M, and t_{ht} = 10 h were obtained by Rietveld refinement using the Fullprof Suite. The results are shown in **Fig. 8** and **Fig. 9**.

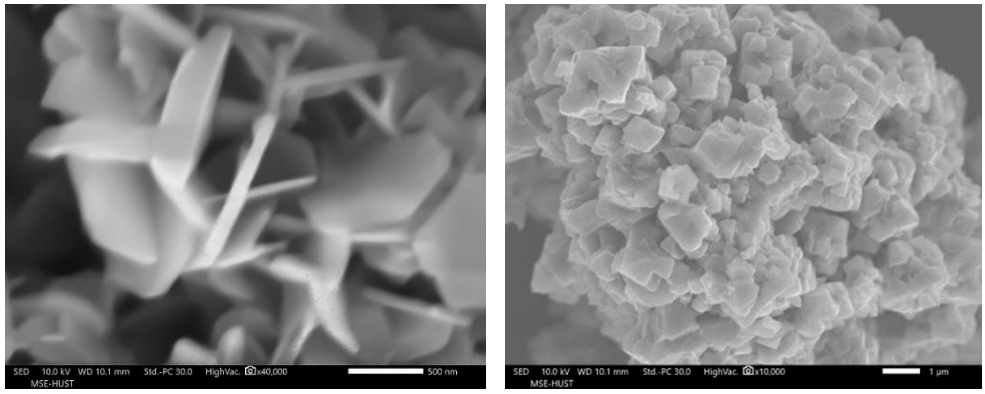

Fig. 7 SEM images of o-$LiMnO_2$ synthesized after 10 h of reaction time.

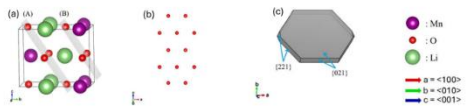

Fig. 8 (a) 3D atomic structures of o-$LiMnO_2$ unit cell, (b) 2D structure of the (021) plane, (c) illustration of o-$LiMnO_2$ crystal shape described only by (221) and (021) planes

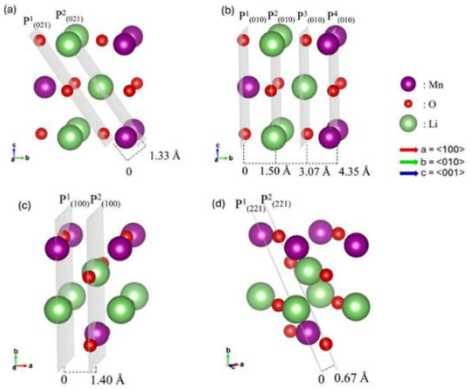

Fig. 9 Schematic illustration showing planes within the a-(021), b-(010), c-(100), and d-(221) interplanar spacing periods (IPSPs).

Fig. 8a shows a unit cell of o-$LiMnO_2$ with the (021) planes made of oxygen atoms with the stacking sequence of ABABAB. The oxygen atoms in these (021) planes form a pseudo-hexagonal arrangement, which is illustrated in **Fig. 8b**. The illustration of the pseudo-hexagonal of o-LiMnO2 provided in **Fig. 8c** is similar to the model of the o-$LiMnO_2$ lattice in previous work [20].

As the faceted morphology of o-$LiMnO_2$ observed in **Fig. 7**, crystal growth of o-$LiMnO_2$ in this work should follow the two-dimensional nucleation mechanism, i.e., surface monolayer clusters must be formed on the plane surface before the growth of crystal can continue. This is because the solid-liquid interface is assumed to be smooth atomically, leading to the difficulty in absorbing atoms in lattice sites [26]. The cluster formation on the plane surface provides steps that reduce the required adsorption energy and increase the attractive forces that improve the adsorption of atoms on those surfaces [27]. Initially, the pseudo-hexagonal layered structure of o-$LiMnO_2$ was formed with growing along the (021) planes to a certain size. After that, because of energy matter, the monolayer clusters of o-$LiMnO_2$ were adsorbed on these (021) planes to facilitate the atom adsorption. To prove this behavior, the planar density ρ of the most four dominant surfaces of o-$LiMnO_2$ structure, i.e., (021), (010), (100), and (221) as shown in Fig. 9 was calculated.

The planar density (PD) of a plane is defined as the number of atoms per unit area on that plane [28]. Lower planar density offers lower surface energy that make the system be more stable and easier to adsorb atoms on that plane [29]. The new method of calculating planar density was used to calculate the position and the planar density of the (021), (010), (100), and (221) planes [30].

Table 2 shows the calculated average planar density of (021), (010), (100), and (221) planes within their IPSPs.

Table 2. The average planar density of o-$LiMnO_2$ crystal.

Plane	(021)	(010)	(100)	(221)
Average PD (atom/Å^2)	0.1316	0.1548	0.1524	0.066

It can be seen that the (021) planes have the second lowest planar density amongst the four, in other words, the (021) planes of o-$LiMnO_2$ can accumulate more critically sized clusters, and thus, growth faster than the (100) and (010) planes. Also, the lower planar density of (221) compared to (021) caused the crystal to grow faster on (221) than (021). As a result, the crystalline structure of o-$LiMnO_2$ shows a pseudo-hexagonal shape as illustrated in Fig. 8c. The SEM images of the o-$LiMnO_2$ (**Fig. 7**) also confirm the formation of a hexagonal shape crystal.

CONCLUSION

Layered structural orthorhombic $LiMnO_2$ was successfully synthesized using $LiOH.H_2O$ and Mn_2O_3 as the raw materials by a one-step hydrothermal process. The variation of hydrothermal temperature, reaction time, and $LiOH.H_2O$ molar concentration in aqueous solutions was difficult to produce high-purity $LiMnO_2$ powder. $LiMnO_2$ powder with the highest purity was synthesized at C_{LH} = 4M, t_{ht} = 8 h, t_r° = 180 °C, and only 90% of the required Mn_2O_3, the remaining Mn_2O_3 in the product was just approx. 0.24%. A layer structure based on the (021) crystal planes of $LiMnO_2$ was obtained from the hydrothermal synthesis, and the crystals of $LiMnO_2$ were pseudo-hexagonal.

REFERENCES

1. Y. Lyu, X. Wu, K. Wang, Z. Feng, T. Cheng, Y. Liu, M. Wang: Advanced Energy Materials, 11(2), 2020, 2000982. https://doi.org/10.1002/aenm.202000982.
2. Zh. Chen, J.R. Dahn: Electrochimica Acta, 49(7), 2004, 1079-1090. https://doi.org/10.1016/j.electacta.2003.10.019.
3. Y. Wang, H.-Y. Shadow Huang: MRS Online Proceedings Library, 530, 2011, 1363. https://doi.org/10.1557/opl.2011.1363.
4. L. Leyssens, B. Vinck, C. Van Der Straeten, F. Wuyts, L. Maes: Toxicology, 387, 2017, 43-46. https://doi.org/10.1016/j.tox.2017.05.015.
5. G.A. Campbell: Mineral Economics, 33(1), 2020, 21-28. https://doi.org/10.1007/s13563-019-00173-8.
6. O.K. Park et al.: Energy & Environmental Science, 4(5), 2011, 1621-1633. https://doi.org/10.1039/C0EE00559B.
7. S. Chen, Z. Gao, T. Sun: Energy Science & Engineering, 9(9), 2021, 1647-1672. https://doi.org/10.1002/ese3.895.
8. H. Zhao et al.: Electrochimica Acta, 166, 2015, 124-133. https://doi.org/10.1016/j.electacta.2015.03.040.
9. M.M. Thackeray, M.F. Mansuetto, J.B. Bates: Journal of Power Sources, 68, 1997, 153-158, 1997. https://doi.org/10.1016/S0378-7753(96)02624-9.
10. G.W. Ling et al.: International Journal of Electrochemical Science, 7(3), 2012, 2455-2467. https://doi.org/10.1016/S1452-3981(23)13893-4.
11. J. Abou-Rjeily, I. Bezza, N.A. Laziz, C. Autret-Lambert, M.T. Sougrati, F. Ghamouss: Energy Storage Materials, 26, 2020, 423-432. https://doi.org/10.1016/j.ensm.2019.11.015.
12. Y. Lyu et al.: Advanced Energy Materials, 11(2), 2021, 2000982. https://doi.org/10.1002/aenm.202000982.
13. A.R. Armstrong, P.G. Bruce: Nature, 381(6582), 1996, 499-500. https://doi.org/10.1038/381499a0.
14. H. Zhou, Y. Li, J. Zhang, W. Kang, Y.W. Denis: Journal of Alloys and Compounds, 659, 2016, 248-254. https://doi.org/10.1016/j.jallcom.2015.11.038.
15. X. Li, Z. Su, Y. Wang: Journal of Alloys and Compounds, 735, 2018, 2182-2189.

https://doi.org/10.1016/j.jallcom.2017.11.384.
16. Z.P. Guo, K. Konstantinov, G.X. Wang, H.K. Liu, S.X. Dou: Journal of Power Sources, 119, 2003, 221-225. https://doi.org/10.1016/S0378-7753(03)00237-4.
17. Y.S. Lee, Y.K. Sun, K. Adachi, M. Yoshio: Electrochimica Acta, 48(8), 2003, 1031-1039. https://doi.org/10.1016/S0013-4686(02)00817-4.
18. Z.P. Guo, G.X. Wang, K. Konstantinov, H.K. Liu, S.X. Dou: Journal of Alloys and Compounds, 346(1-2), 2002, 255-259. https://doi.org/10.1016/S0925-8388(02)00498-X.
19. Y. Zheng, X. Hao, J. Niu, B. Pan: Materials Letters, 163, 2016, 98-101. https://doi.org/10.1016/j.matlet.2015.10.042.
20. Reimers J.N., Fuller E.W., Rossen E. and Dahn J.R.: Journal of the Electrochemical Society, 140(12), 1993, 3396. https://doi.org/10.1149/1.2221101.
21. L. Croguennec, P. Deniard, R. Brec: Journal of The Electrochemical Society, 144(10), 1997, 3323. https://doi.org/10.1149/1.1838013.
22. Y.S. Lee, M. Yoshio: Electrochemical and Solid-State Letters, 4(10), 2001, A166. https://doi.org/10.1149/1.1399879.
23. O. Fukunaga, K. Takahashi, T. Fujita, J. Yoshimoto: Materials Research Bulletin, 4(5), 1969, 315-322. https://doi.org/10.1016/0025-5408(69)90035-X.
24. S.T. Myung, S. Komaba, N. Kumagai: Electrochimica Acta, 47(20), 2002, 3287-3295. https://doi.org/10.1016/S0013-4686(02)00248-7.
25. S. Komaba et al.: Solid State Ionics, 152, 2002, 311-318. https://doi.org/10.1016/S0167-2738(02)00320-X.
26. R.P. Liu, W.K. Wang, D. Li, D.M. Herlach: Scripta Materialia, 41(8), 1999, 855-860. https://doi.org/10.1016/S1359-6462(99)00218-3.
27. S. Vasudevan, S. Nagalingam, R. Dhanasekaran, P. Ramasamy: Kristall und Technik, 16(3), 1981, 293-297. https://doi.org/10.1002/crat.19810160303.
28. G.A. Chadwick: Metal Science Journal, 1(1), 1967, 132-139. https://doi.org/10.1179/msc.1967.1.1.132.
29. A. Bravais: *Etudes Cristallographiques*, Paris: Gauthier-Villars, 1866.
30. Q. Fan: Journal of Applied Crystallography, 49(5), 2016, 1454-1458. https://doi.org/10.1107/S1600576716010827.
31. L. Meng et al.: Journal of Rare Earths, 36(2), 2018. https://doi.org/10.1016/j.jre.2017.05.017.
32. B.H. Toby: Powder diffraction, 21(1), 2006, 67-70. https://doi.org/10.1154/1.2179804.
33. E. Prince: *Mathematical techniques in crystallography and materials science*, 3rd edition, Berlin: Springer, 2004. https://doi.org/10.1007/978-3-642-18711-7.
34. R.A. Young: *Introduction to the Rietveld method*, Oxford: Oxford Science Publication, 1993.